This is the accepted version of the article published in the final form in Nanoscale (2021, online publisher version available from 15.11.2021) by RSC
DOI: 10.1039/D1NR06974H
http://xlink.rsc.org/?DOI=D1NR06974H
https://doi.org/10.1039/D1NR06974H

ARTICLE

Supramolecular organization of melem for the synthesis of photoactive porous carbon nitride rods

Received 00th January 20xx,
Accepted 00th January 20xx

DOI: 10.1039/x0xx00000x

Jiawei Xia,[a,b] Gabriel Mark,[b] Michael Volokh,[b] Yuanxing Fang,[c] Haiqun Chen,[a] Xinchen Wang[c] and Menny Shalom[b]*

Intrinsic defects and structural properties are two main factors influencing the photocatalytic performance of carbon nitride (CN) materials. Here, photoactive porous CN rods are fabricated through the thermal condensation of melem-based hexagonal supramolecular assemblies. To overcome the poor solubility of melem, we exfoliate the bulk melem using hydrochloric acid. The latter allows good dispersibility of the monomer in an aqueous medium, leading to the formation of H-bond bridged supramolecular assembly with good regularity in both size and rod-like morphology. After thermal condensation, a well-ordered structure of porous CN rods with fewer defects due to the high thermal stability of the melem-based supramolecular assembly is obtained. The new CN materials have high specific surface area, good light-harvesting properties, and enhanced charge separation and migration. The optimal CN material exhibits excellent photocatalytic activity and durability towards hydrogen evolution reaction (HER) and CO_2 reduction reaction (CO_2RR, with good selectivity).

Introduction

Carbon nitride (CN) has emerged as a promising metal-free photocatalyst for a wide range of applications.[1,2] Bulk CN presents some drawbacks in practical applications, such as low accessible surface active sites and poor charge separation efficiency.[3,4] Among other factors, its defects and structural properties significantly influence its photocatalytic performance.[5–8] This observation has motivated efforts to develop synthetic methods to control those parameters. In particular, the utilization of supramolecular assemblies composed of CN monomers as reactants has been explored as a bottom-up strategy for the simple and controllable synthesis of CN materials with unique physicochemical structure and functionality.[9–11] The categories of supramolecular assemblies reported so far have generally been restricted to those involving small N-rich monomers such as melamine, dicyandiamide, and their analogs.[12–14]

Melem is an important intermediate to graphitic carbon nitride and is commonly obtained from the self-condensation of melamine.[15,16] Its large aromatic tricyclic unit, C_6N_7, usually denoted as *s*-heptazine or tri-*s*-triazine,[17] is the basic repeating unit in graphitic CN materials. It is thermally stable up to 400–450 °C,[18] which is high compared with related aromatic motifs and other small N-rich monomers. The good thermal stability suppresses the massive sublimation that these small CN monomers undergo during the condensation process. This is also expected to be beneficial in reducing the number of defects in the CN material.[19] Therefore, though less reported, the synthesis of CN from melem has great potential, especially through a supramolecular assembly approach.

Melem units can form structurally ordered supramolecular assemblies based on hydrogen bonds.[20–23] However, the poor dispersibility of melem in many solvents—even under intense sonication—limits its exploitation in supramolecular assemblies and hence the possibility of constructing a well-ordered supramolecular structure with uniform morphology. Inspired by the electrostatic re-assembly of CN nanosheets via acidic exfoliation of bulk CN material,[24–26] we hypothesized that a proper acid pretreatment could constitute a good strategy for the solubilization/dispersion of regular supramolecular precursor.

In this work, we designed a simple bottom-up method for the construction of CN rods that are more porous and have fewer defects than conventional CN via the condensation of a supramolecular assembly consisting of melem units. The exfoliation of melem by hydrochloric acid (HCl) results in good dispersibility in water. As HCl is removed, the melem units self-assemble to form well-regulated hexagonal rods bridged by H-bonds, which helps control the morphology and structure, and thus the catalytic properties of the target CN product. The optimal CN material shows good photocatalytic activity and cycling performance towards both the hydrogen evolution reaction (HER) and the CO_2 reduction reaction (CO_2RR, also with good selectivity).

Results and discussion

[a] Key Laboratory of Advanced Catalytic Materials and Technology, Advanced Catalysis and Green Manufacturing Collaborative Innovation Center, Changzhou University, Changzhou, Jiangsu Province 213164, China.
[b] Department of Chemistry and Ilse Katz Institute for Nanoscale Science and Technology, Ben-Gurion University of the Negev, Beer-Sheva 8410501, Israel. E-mail: mennysh@bgu.ac.il.
[c] State Key Laboratory of Photocatalysis on Energy and Environment College of Chemistry, Fuzhou University, Fuzhou 350116, China.
Electronic Supplementary Information (ESI) available: [Additonal Me, $MeCl_x$, and melem+HCl characterization (SEM, XRD, FTIR, XPS, zeta-potential), characterization of the resulting CN materials (SEM, N_2 sorption, XRD, XPS, FTIR, PL), photocatalytic activity analysis (HER of different CNs and conditions; stability for HER and CO_2RR: TEM, XRD, FTIR), Mott-Schottky plots, and HER CN photocatalysts comparison table]. See DOI: 10.1039/x0xx00000x

Bulk melem, consisting of large irregular aggregates, was synthesized by direct heating melamine powder to 425 °C (Fig. 1a). After that, we dispersed the obtained melem in water and submitted the resulting suspension to overnight shaking to rearrange the melem units bridged by H-bonds, giving rise to its morphological transformation into hexagonal rods (Fig. S1). Pretreating bulk melem with an aqueous HCl solution increases its dispersibility in water. As HCl is removed by washing, the well-dispersed melem molecules reorganize into a hexagonal rod-like supramolecular assembly with an ordered structure and a regular morphology (Fig. 1b–c and Fig. S2). The changes in the XRD diffraction pattern (in the 2θ ranges of 5~15° and 25~30°) corroborate the crystal rearrangement of melem (Fig. 1d).[27] The dispersibility of melem is considered one of the determining factors for the structural and morphological properties of the supramolecular assembly; indeed, the pretreatment in a more concentrated HCl solution affords sufficient exfoliation of bulk melem to yield a more regular morphology of hexagonal rods (Fig. 1b–c and Fig. S2e–h). The samples were prepared using various volume ratios of concentrated HCl solution/total aqueous solution volume: 0/1, 0.2/1, 0.4/1, 0.6/1, 0.8/1 and 1/1, labelled as $MeCl_x$; for example, $MeCl_{1.0}$ is a volume ratio of 1/1 for a concentrated HCl solution/total aqueous solution volume. These supramolecular assemblies, prepared from a concentrated HCl solution/total aqueous solution volume ratio of 0.4 and above ($MeCl_x$, $x \geq 0.4$) all show similar XRD features (Fig. S3a). Moreover, the XRD spectra indicate that the $MeCl_{1.0}$ assembly structure is not altered even with a pretreatment time of over 4 h in concentrated HCl (Fig. S3b). The FTIR spectra show an obvious decrease in peak intensity for the signals above 3300 cm^{-1}, corresponding to N–H vibration in the edge amino groups, which discloses the establishment of an H-bond network in all supramolecular assemblies (Fig. 1e and Fig. S4).[19,21]

In order to study the interaction between melem and the product of HCl dissolution, pretreated melem with concentrated HCl solution was centrifugated and dried directly without water washing; the resulting sample is henceforth labeled as melem+HCl. It shows a completely different morphology from that of $MeCl_x$ (Fig. S5), stemming from its distinct crystal structure (Fig. S6a). The disappearance of the two sharp peaks above 3300 cm^{-1} indicates an interaction between HCl and melem molecules, which hinders the vibration of amino groups (Fig. S6b). Unlike the melem+HCl precursor, which contains a large amount of Cl species, $MeCl_{1.0}$ shows the same survey XPS spectrum as that of untreated Me (melem self-assemblies in water without HCl pretreatment), confirming the near-complete removal of Cl after the washing process (Fig. S7). Furthermore, Me and $MeCl_{1.0}$ also exhibit essentially the same C 1s and N 1s high-resolution XPS spectra (Fig. S8). Zeta-potentials were measured at 25 °C in aqueous suspensions, using the Smoluchowski model (Fig. S9). The measured values are practically similar (around –8.7 mV) for both Me (suspension pH: ~7.02) and $MeCl_{1.0}$ (suspension pH: ~6.96), reflecting the close resemblance of their surface electric properties. The melem+HCl sample (suspension pH: ~3.66), on the other hand, has a significantly more positive zeta potential (35.9 mV). We ascribe this positive charge to the positively charged melemium anion resulting from the protonation of melem by HCl.[28] Hence, it can be inferred that the reaction between melem and HCl is reversible, where HCl can be removed with a large amount of water. After the removal of water, $MeCl_{1.0}$ shows the same supramolecular structure as that of Me.

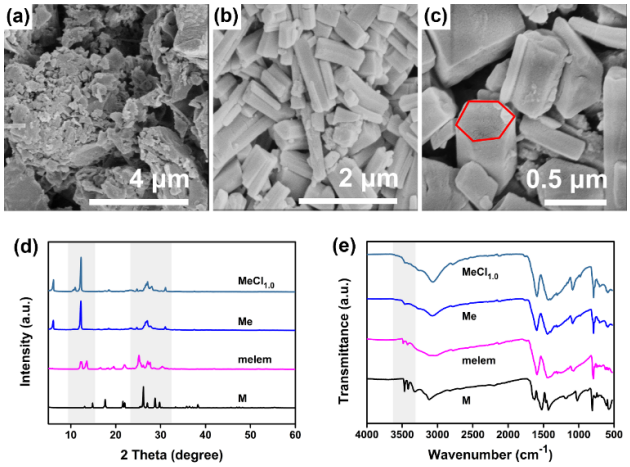

Fig. 1 Scanning electron microscopy (SEM) images of (a) melem, (b, c) $MeCl_{1.0}$ at two different magnifications; (d) XRD patterns, and (e) FTIR spectra of different precursors (M = melamine, melem, Me = melem supramolecular assembly in aqueous medium, $MeCl_{1.0}$ = melem pretreated with a concentrated HCl solution, followed by supramolecular assembly via water washing to remove HCl).

Based on the results above, a possible mechanism of the synthesis of porous CN rods is proposed (Fig. 2). As observed with other acids,[29,30] protonation occurs on the heptazine-ring's N atoms of the melem units. Electrostatic repulsion between the protonated melem units ensures their aqueous dispersibility. As the HCl is removed by washing with DI water, the homogeneously dispersed melem units are gradually deprotonated into neutral melem, thus reducing the electrostatic repulsion and allowing the melem units to reorganize into their final H-bond-based self-assemblies with a regular hexagonal-rod morphology. Consequently, the target porous CN rods are obtained via a facile thermal condensation process in air. The CN material synthesized via direct thermal polymerization of melamine powder in air (CN-M) shows a morphology of large irregular blocks with a low Brunauer-Emmett-Teller (BET) specific surface area of 11.3 $m^2\ g^{-1}$. Using melem as a precursor produces CN sheets (CN-melem) with a slightly more porous structure together with a decrease in both size and thickness, translating into an increased BET specific surface area of 14.0 $m^2\ g^{-1}$. The thermal condensation of a supramolecular assembly of either bulk melem or HCl-pretreated melem in water leads to a CN material with a porous structure. To identify different CN samples, "CN-" is added in front of each precursor. CN-$MeCl_{1.0}$ manifests the largest BET specific surface area, 57.8 $m^2\ g^{-1}$, which is beneficial for light-harvesting and is expected to improve photocatalytic activity (Fig. 3a–d, Fig. S10, and Fig. S11). Pretreating melem with higher concentrations of HCl enables a better dispersion. As the melem molecules get neutralized by washing with DI water to remove the HCl species, they self-assemble via H-bonds into rods with an improved regularity, leading to a more uniform morphology of the target CN product (Fig. S12). The XRD patterns show two diffraction peaks related to the (100) and (002) planes centered at 2θ of 13.0° and 27.4° (Fig. 3e), which are assigned to the in-plane structural packing motif of heptazine units

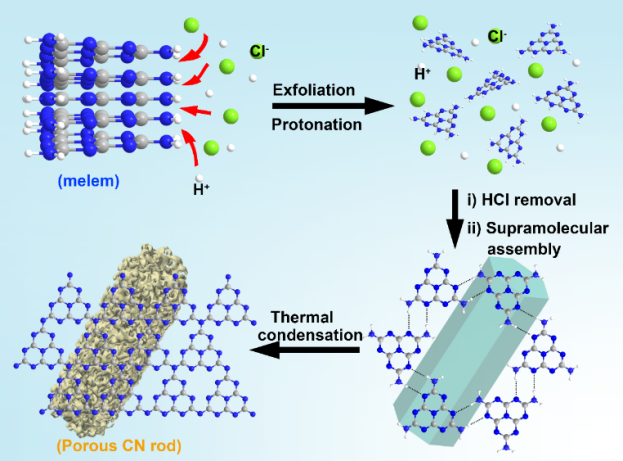

Fig. 2 Schematic illustration of porous CN rod synthesis from a supramolecular assembly of melem and hydrochloric acid.

and the characteristic interlayer aromatic stacking reflection of CN layers, respectively.[31,32] The gradually decreasing intensity and increasing width of the (002) plane from CN-M, CN-melem, CN-Me, to CN-$MeCl_{1.0}$ reflect the improved periodicity of the heptazine units and the reduced stacking number of CN layers.[33] As inferred from the gradually decreasing peak corresponding to the (002) plane in Fig. S13a, a CN sample with thinner layers (in an average exfoliated flake) is obtained when melem is pretreated at higher HCl concentrations. A plausible mechanism of the exfoliation would be that the electrostatic repulsion of positively charged protonated melem moieties increases the intermolecular distances, permitting a better supramolecular reorganization after the removal of HCl species. Additionally, changing the shaking time in the melem pretreatment (from 4 to 24 h; identical HCl concentration) does not result in any remarkable difference in the XRD patterns of the CN samples (Fig. S13b), indicating that the samples obtained after 4 hours already reach their final state; hence, at least after this period, the HCl concentration is the main factor that influences the structural property of the target CN material. In all cases, the investigated CN materials exhibit similar C 1s and N 1s high-resolution XPS spectra, which match well with the typical melon-based CN materials (Fig. S14). The C species exist in the forms of sp^2 C=C (Binding energy (BE) of 284.8 eV) from the carbonaceous environment, C=N–C (BE = 288.1 eV) coordination in the CN framework, C–NH_2 (BE = 286.4 eV) on the edge of heptazine units, and C–O (BE = 289.0 eV) caused by the introduction of oxygen from the atmosphere during the thermal condensation process.[34,35] The N 1s spectra can be well deconvoluted into three peaks at BEs of 398.6, 399.8, and 401.0 eV, corresponding to C=N–C, N–$(C)_3$, and C–NH, respectively.[36–38] The optical properties of the obtained CN materials were first characterized by FTIR, as shown in Fig. 3f and Fig. S15. All CN products show a broad peak in the region of 2800–3500 cm^{-1}, assigned to the stretching vibration mode of N–H.[39] In this same region, the sharper peaks of CN-Me and CN-$MeCl_{1.0}$, relative to CN-M and CN-melem, suggest a more ordered packing of the remaining amino groups at the terminating heptazine edges.[21] The group of peaks located at 1200–1700 cm^{-1} corresponds to the stretching mode of CN heterocycles. The peak at ~800 cm^{-1} represents the breathing vibration of the heptazine units in the CN framework, where the detected stronger peaks of CN-Me and CN-$MeCl_{1.0}$ reflect a more ordered repetition of heptazine units in the inner CN layer.[40] UV–vis absorbance spectra show that the CN materials (CN-Me and CN-$MeCl_{1.0}$) synthesized from supramolecular precursors have a slightly broadened light absorption, with a smaller bandgap (E_g) of approximately 2.78 eV (Fig. 3g). The photoluminescence (PL) spectrum in Fig. 3h reveals a pronounced quenching for CN-$MeCl_{1.0}$ compared to the reference CN samples and a shorter lifetime (Fig. S16 and Table S1), implying an alternative, non-radiative photogenerated charge recombination pathway.[41,42] This is benefitted from ordered structure and good thermal stability of the supramolecular assembly that can lead to the formation of porous CN material with fewer defects, more ordered structure, and thinner latyers for enhanced charge separation.[19]

The photocatalytic activity was first evaluated by performing HER in the presence of 10 vol.% of triethanolamine (TEOA) as the hole scavenger and 3 wt.% of Pt as a co-catalyst. CN-M and CN-melem show relatively low H_2 evolution rates: only 437 and 641 μmol h^{-1} g^{-1}, respectively (Fig. 4a and Fig. S17). The value increases to 1557 μmol h^{-1} g^{-1} for CN-Me, a CN from a melem reorganized in water before calcination. Pretreating the melem with HCl solution to influence the supramolecular assembly results in a substantial enhancement of H_2 generation by the final CN photocatalysts. CN-$MeCl_{1.0}$ exhibits the highest HER rate (4764 μmol h^{-1} g^{-1}), thanks to its higher specific surface area and better light adsorption. The apparent quantum efficiency (AQE) value at 405 nm was measured to be 6.8%, the highest among the investigated CN samples (Fig. 4a). As listed in Table S2, the photocatalytic activity of CN-$MeCl_{1.0}$ is superior to that of various reported CN materials synthesized from

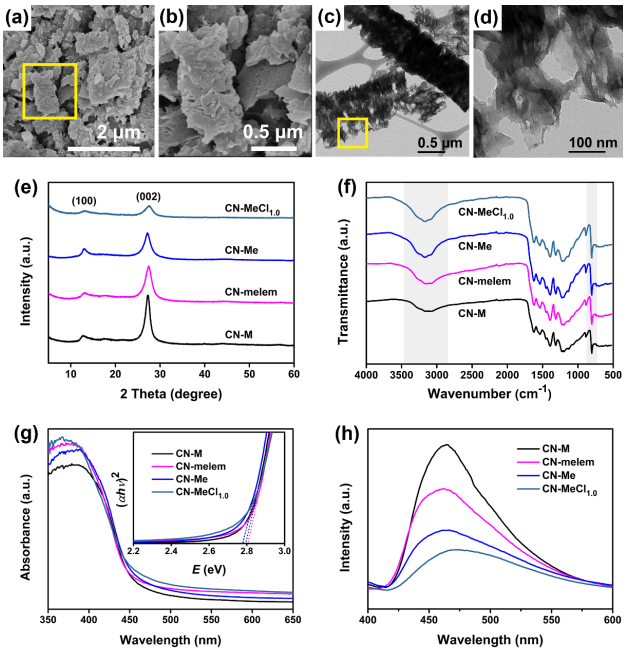

Fig. 3 (a, b) SEM images and (c, d) Transmission electron microscopy (TEM) images of CN-$MeCl_{1.0}$ at different magnifications; (e) XRD patterns, (f) FTIR spectra, (g) UV–vis spectra (inset: Tauc plot analysis), and (h) PL emission spectra (excitation wavelength: 370 nm) of different CN materials.

melamine as the starting monomer. Furthermore, CN-MeCl$_{1.0}$ also exhibits excellent stability towards HER after five consecutive 3-h uses (Fig. 4b), maintaining its morphology and porous structure (Fig. S18). The photodeposited Pt cubes are uniformly dispersed on the CN's surface after the stability test, with an average size of 7.6 nm and a narrow size distribution, which favors good photocatalytic performance. To optimize the conditions of the supramolecular assembly, we investigated the influence of both the HCl concentration and the overall shaking time in the melem pretreatment. The HER performance of the relevant CN samples is shown in Fig. S19–S20. The H_2 generation rate shows a positive correlation with the concentration of the HCl pretreatment solution. Interestingly, whereas XRD analysis suggested that all CN-MeCl$_{1.0}$ samples prepared using shaking times of 4 hours or more are structurally identical, this experiment revealed an apparent influence of the shaking time on the HER rate. However, the samples prepared with a 24 h shaking period did not show a significant improvement; for that reason, we consider a 16 h shaking period in a concentrated aqueous HCl solution to be the optimal condition to form supramolecular assemblies towards the most photoactive CN. For the HER photocatalytic reaction, Pt nanoparticles are in-situ photoreduced onto the surface of the CN layer as the cocatalyst by using H_2PtCl_6 as the Pt source. The photogenerated electrons of the CN transfer to the Pt particles, providing active sites for H_2 evolution. Meanwhile, TEOA—the hole scavenger—is oxidized by the remaining photogenerated holes.[43]

Further evaluation of the activity of the CN materials consisted of a photocatalytic CO_2RR in a mixture of H_2O and MeCN containing TEOA as the hole scavenger and cobalt(II) bipyridine ([Co(bpy)$_3^{2+}$]) as a co-catalyst. No CO was detected by gass chromatography (GC) when the reaction was conducted in the dark, confirming the photocatalytic nature of the mechanism. No CO was detected in an Ar atmosphere under light irradiation either, confirming that CO originates from the CO_2 reactant rather than another substance in

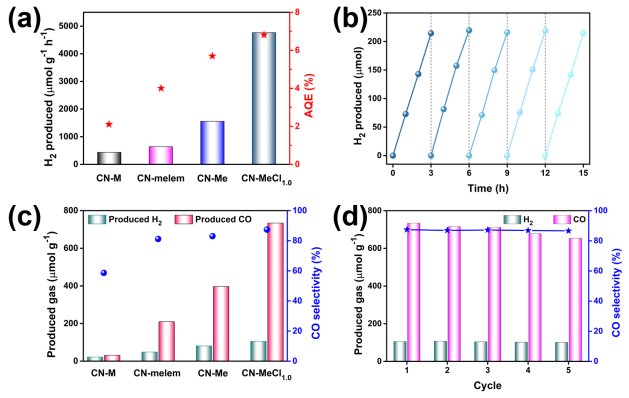

Fig. 4 Photocatalytic characterization. (a) HER performance of different CN materials. The AQY values were measured under monochromatic light irradiation at λ = 405 nm; (b) HER stability of CN-MeCl$_{1.0}$; (c) CO_2RR performance of different CN materials; (d) CO_2RR stability of CN-MeCl$_{1.0}$. Reaction conditions: for HER: CN powder (15 mg), H_2O (17.1 mL), TEOA (1.9 mL), H_2PtCl_6 (3 wt.% Pt), 25 °C, 600 rpm, 100 W white LED (λ > 410 nm); for CO_2RR: CN powder (30 mg), MeCN (4 mL), H_2O (1 mL), TEOA (1 mL), bpy (15 mg), $CoCl_2$ (1 µmol), 30 °C, 1000 rpm, 100 W white LED (λ > 410 nm).

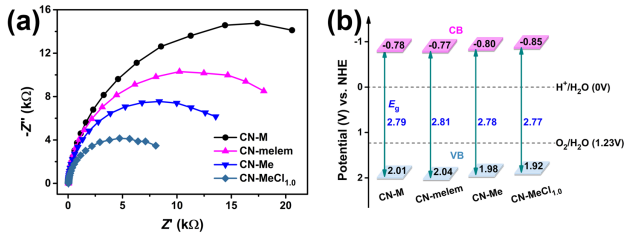

Fig. 5 (a) Nyquist plots (at –0.1 V *vs.* Ag/AgCl) of different CN materials in 0.1 M Na_2SO_4 aqueous solution; (b) schematic illustration of the proposed energy band diagram for the CN materials based on a Mott-Schottky analysis and the calculated optical bandgaps.

the system. During a 3 h reaction with CO_2 over different CN materials under light irradiation, CO was detected as the primary reduction product, along with a small portion of H_2 as the byproduct (Fig. 4c and Fig. S21). As expected, the CN-MeCl$_{1.0}$ sample gives the highest CO generation rate, 734 µmol g^{-1}, which is 23.7-fold higher than that of CN-M (31 µmol g^{-1}). It also exhibits the highest selectivity of 87.4% towards CO, compared to the reference CN samples (Fig. 4c). To evaluate the cycling performance of the catalyst, we collected the CN-MeCl$_{1.0}$ powder from the reaction system via filtration, washed it with MeCN, and finally dried it for the next use. As shown in Fig. 4d, CN-MeCl$_{1.0}$ displays desirable stability: it maintains its selectivity towards CO generation after 5 cycles. Additionally, the morphology and porous structure of the catalyst remains unchanged after this cycling study (Fig. S22). In this reaction system, $CoCl_2$ and bpy form [Co(bpy)$_3^{2+}$] as the cocatalyst. The photogenerated electrons are transferred to the [Co(bpy)$_3^{2+}$], which serves as the electron mediator to activate Co(II) to Co(0) for CO_2 binding, followed by the desirable reduction of CO_2 to CO that accompanies a recovery of the cobalt complex. Additional detailed mechanism investigation appears in previous works from our groups and others.[21,44,45]

Electrochemical impedance spectroscopy (EIS) of CN-MeCl$_{1.0}$ shows that it has the smallest Nyquist plots diameter of all studied materials and thus the lowest barrier to photoinduced charge carrier mobility (Fig. 5a). The investigated CN materials exhibit an n-type behavior according to the Mott-Schottky measurements (Fig. S23). The calculated band positions are illustrated in Fig. 5b, where CN-MeCl$_{1.0}$ has the most negative conduction band (CB) among the investigated CN samples, manifesting a favorable thermodynamic driving force for both HER and CO_2RR.[46,47]

Conclusions

In summary, we demonstrated that the pretreatment of bulk melem with aqueous HCl solution leads to a significant increase in its dispersibility, which in turn allows the facile construction of supramolecular assemblies. The exfoliation degree of melem mainly depends on the concentration of the HCl solution, which plays an essential role in the formation of rod-like supramolecular assemblies with regular morphologies and structures. After thermal condensation in air, the obtained CN materials consist of a thin layer of a porous rod-like structure with increased repetition of basic heptazine units and a larger specific surface area compared to bulk CN (CN-M). The optimal sample, CN-MeCl$_{1.0}$, exhibits excellent

photocatalytic activity towards HER (H_2 generation rate of 4764 µmol h^{-1} g^{-1}) and CO_2RR (CO production of 734 µmol g^{-1} within 3 h), which is ~10.9 and ~23.7 times higher than that of bulk CN, respectively. It further shows satisfactory stability and selectivity for both reactions.

Experimental section

Materials and reagents

All chemicals were purchased from the indicated commercial vendors and used as received. Deionized (DI) water used for all experiments was processed in a Millipore Direct-Q system (18.2 MΩ cm resistivity). Melamine (M, 99%), chloroplatinic acid solution (8 wt.% H_2PtCl_6 in H_2O), cobalt (II) chloride hexahydrate ($CoCl_2{\cdot}6H_2O$, 98% ACS), and Nafion perfluorinated resin solution (5 wt.% in lower aliphatic alcohols and water) from Sigma-Aldrich; hydrochloric acid (HCl, 32 wt.%, AR) from Bio-Lab, Israel; triethanolamine (TEOA, 99%) from Carl Roth; 2,2'-bipyridine (bpy, 99+%) from Alfa Aesar; ethylene glycol (EG, ≥99.5%) from Merck; acetonitrile (MeCN, HPLC solvent) and anhydrous sodium sulfate (Na_2SO_4, 99%) from J. T. Baker.

Synthesis of CN catalysts

Melem was synthesized by direct thermal condensation of melamine powder in a lidded ceramic crucible at 425 °C for 12 h under N_2 atmosphere (425 °C was reached at a heating rate of 5 °C min^{-1} from room temperature). After it was let to cool down to room temperature, the resulting melem was carefully ground into a fine powder for subsequent use. For a typical exfoliation experiment, 0.5 g of melem was first dispersed in 25 mL of HCl aqueous solution by sonication for 15 min in a sealed centrifuge tube to yield a uniform suspension (samples were prepared using various volume ratios of concentrated HCl solution/total aqueous solution volume: 0/1, 0.2/1, 0.4/1, 0.6/1, 0.8/1 and 1/1). After shaking for 16 h (unless stated otherwise), the residue was collected, washed with DI water to remove HCl until neutral by centrifugation, and then dried at 40 °C in a vacuum oven. The obtained precursors were labelled as Me, $MeCl_{0.2}$, $MeCl_{0.4}$, $MeCl_{0.6}$, $MeCl_{0.8}$, and $MeCl_{1.0}$, respectively. In addition, to study the influence of the preliminary treatment duration on the structural and morphological properties of the supramolecular assemblies, we submitted bulk melem to various shaking times (4, 8, 12, and 24 h) in the concentrated HCl solution. The obtained solid precursors were collected following the same procedure stated above.

Carbon nitride materials were synthesized via thermal polymerization of the as-prepared supramolecular assemblies at 550 °C for 4 h in a muffle furnace (reached at a heating rate of 5 °C min^{-1} from room temperature). As a label for each CN product, "CN-" was added in front of the name of the corresponding supramolecular precursor (CN-Me, CN-$MeCl_{1.0}$, *etc.*). For comparison, two reference CN products labeled as CN-M and CN-melem were synthesized by directly heating melamine or melem powder under the same conditions.

Characterization

The morphology of the materials was characterized by scanning electron microscopy (SEM, FEI Verios 460L equipped with a FEG source operated at U_0 = 3.0 kV), and transmission electron microscopy (TEM, Tecnai T12 G² TWIN, operated at U_0 = 120 kV). X-ray powder diffraction (XRD) patterns were recorded on a Panalytical Empyrean powder diffractometer (position sensitive detector X'Celerator, operation parameters: Cu K_α, λ = 1.54178 Å, 40 kV, 30 mA) with a scanning range of 2θ between 5° and 60°. X-ray photoelectron spectroscopy (XPS) was performed on a Thermo Fisher Scientific ESCALAB 250 (K_α, 1486.6 eV). Optical properties: light absorption was characterized using a diffuse reflectance accessory on a Cary 100 spectrophotometer; optical band gap was estimated using a Tauc plot analysis of these spectra. Fourier-transform infrared spectroscopy (FTIR) was obtained on a Thermo Scientific Nicolet iS5 (KBr window, diamond iD7 ATR optical base). Photoluminescence (PL) spectra were recorded on a FluoroMax® 4 spectrofluorometer (Horiba Scientific) excited at a wavelength of 370 nm. Time-resolved fluorescence measurements were performed on a time-correlated single-photon counting (TCSPC) setup with a Horiba Fluorolog modular spectrofluorometer. The PL lifetimes ($\tau_{av.}$) were estimated from time-resolved PL spectra decay curves fitted to a triple-exponential function: $\tau = \sum_{i=1}^{i=n} A_i \tau_i^2 / \sum_{i=1}^{i=n} A_i \tau_i$, where τ_i is the lifetime and A_i is the amplitude of the i^{th} component. The apparent specific surface area of the CN materials was measured on a Quantachrome Autosorb IQ2 at 77 K. The values were calculated based on the Brunauer-Emmett-Teller (BET) model applied to the isotherm data points of the adsorption branch in nitrogen adsorption-desorption experiments. Electrochemical impedance spectroscopy (EIS) and Mott-Schottky analysis of CN products were measured on an Autolab potentiostat (Metrohm, PGSTAT302N) using a three-electrode system with a Pt plate (1.0 cm × 1.0 cm), a Ag/AgCl (saturated KCl) electrode, and a fluorine-doped tin oxide-coated glass (FTO; Xop glass (Xop Física S. L., Spain)-supported CN film as the counter, reference, and working electrodes, respectively. To the FTO surface, a fresh paste composed of 120 µL of EG, 20 µL of Nafion solution, and 30 mg of the respective CN catalyst was coated using the doctor-blade technique.[22] Here, scotch tape (3M company) was used to shape the profile of the CN film and control its thickness. After the removal of the scotch tape and the evaporation of EG on a heating plate, the working electrode was obtained. Zeta-potentials were measured on Malvern Nano ZS at room temperature.

Catalytic performance test of CN materials

Photocatalytic hydrogen evolution reaction (HER)

The hydrogen evolution reaction was carried out in a sealed quartz vessel held by a jacked beaker in a water bath under a controlled temperature of 25 °C. Typically, 15 mg of CN material was dispersed via sonication in a mixed solution composed of 17.1 mL of DI water, 1.9 mL of TEOA as the hole scavenger, and a certain amount of H_2PtCl_6 solution (3 wt.% Pt). After the vessel was purged with Ar to remove residual air, Pt co-catalyst nanoparticles were in-situ photodeposited on the surface of the CN catalyst under white LED light irradiation (Bridgelux BXRA-50C5300, 100 W, λ > 410 nm) for 30 min under continuous stirring (600 rpm). At these conditions, the amount of generated H_2 gas was monitored every 1 h through gas chromatography (Agilent 7820 GC system). The apparent quantum efficiency (AQE) of each CN material was measured under monochromatic light irradiation (Thorlabs mounted LEDs, λ = 405, 430, and 455 nm, respectively), where the amount of generated H_2 in the sealed reactor was monitored automatically, on-line, with an Ar line connected to the Agilent 7820 GC system. The AQE values were calculated according to the following equation:

$$AQE = \frac{2 \times \text{Number of evolved } H_2 \text{ molecules}}{\text{Number of incident photons}} \times 100\% \quad (1)$$

Photocatalytic CO_2 reduction reaction (CO_2RR)

The same reaction setup was used to check the photocatalytic activity of the as-synthesized CN materials towards CO_2RR. The reaction mixture was composed of 30 mg of CN catalyst, 4 mL of MeCN, 1 mL of DI water as the proton donor, 1 mL of TEOA as the hole scavenger, 15 mg of bpy, and 1 µmol of $CoCl_2$ as a co-catalyst. After sonication to yield a homogeneous suspension, the vessel was purged with CO_2 (99.9%) to remove the air. The same 100 W white LED array was employed as the light source and the reaction was carried out under continuous stirring (1000 rpm) at 30 °C. The amount of generated gas was analyzed every 1 h by gas chromatography (Agilent 7820 GC system equipped with a thermal conductivity detector—TCD).

Author Contributions

Jiawei Xia: experiments, data analysis, writing of the original draft.
Gabriel Mark: characterization.
Michael Volokh, Yuanxing Fang, Xinchen Wang, Haiqun Chen: characterization, revision.
Menny Shalom: Data curation, revision, supervision.

Conflicts of interest

The authors declare no conflict of interest.

Acknowledgements

This project was received funding from the European Research Council (ERC) under the European Union's Horizon 2020 Research and Innovation Programme (Grant Agreement No. 849038). This work was also financially supported by the joint Israel Science Foundation-National Science Foundation of China (ISF-NSFC) Grant No. 2969/19, National Natural Science Foundation of China (21961142019 and 22075047). The authors thank Jonathan Tzadikov, Rotem Geva, Liel Abisdris, Ayelet Tashakory, and Junyi Li (Ben-Gurion University of the Negev) for technical support.

References

1 G. Li, Z. Xie, S. Chai, X. Chen, X. Wang, *Appl. Catal. B*, 2021, **283**, 119637.
2 W. Wang, C. Zhou, Y. Yang, G. Zeng, C. Zhang, Y. Zhou, J. Yang, D. Huang, H. Wang, W. Xiong, X. Li, Y. Fu, Z. Wang, Q. He, M. Jia, H. Luo, *Chem. Eng. J.*, 2021, **404**, 126540.
3 Y. Xiao, G. Tian, W. Li, Y. Xie, B. Jiang, C. Tian, D. Zhao, H. Fu, *J. Am. Chem. Soc.*, 2019, **141**, 2508.
4 H. Wang, B. Wang, Y. Bian, L. Dai, *ACS Appl. Mater. Interfaces*, 2017, **9**, 21730.
5 J. Yang, H. Wang, L. Jiang, H. Yu, Y. Zhao, H. Chen, X. Yuan, J. Liang, H. Li, Z. Wu, *Chem. Eng. J.*, 2022, **427**, 130991.
6 C. Hu, F. Chen, Y. Wang, N. Tian, T. Ma, Y. Zhang, H. Huang, *Adv. Mater.*, 2021, **33**, e2101751.
7 Q. Hao, G. Jia, W. Wei, A. Vinu, Y. Wang, H. Arandiyan, B. -J. Ni, *Nano Res.*, 2019, **13**, 18.
8 Z. Tong, L. Huang, H. Liu, W. Lei, H. Zhang, S. Zhang, Q. Jia, *Adv. Funct. Mater.*, 2021, **31**, 2010455.
9 C. Zhao, Q. Li, Y. Xie, L. Zhang, X. Xiao, D. Wang, Y. Jiao, C. A. Hurd Price, B. Jiang, J. Liu, *J. Mater. Chem. A*, 2020, **8**, 305.
10 S. Wang, H. Zhao, X. Zhao, J. Zhang, Z. Ao, P. Dong, F. He, H. Wu, X. Xu, L. Shi, C. Zhao, S. Wang, H. Sun, *Chem. Eng. J.*, 2020, **381**, 122593.
11 F. Zhang, J. Li, H. Wang, Y. Li, Y. Liu, Q. Qian, X. Jin, X. Wang, J. Zhang, G. Zhang, *Appl. Catal. B*, 2020, **269**, 118772.
12 J. Barrio, M. Shalom, *ChemCatChem*, 2018, **10**, 5573.
13 Q. Liang, B. Shao, S. Tong, Z. Liu, L. Tang, Y. Liu, M. Cheng, Q. He, T. Wu, Y. Pan, J. Huang, Z. Peng, *Chem. Eng. J.*, 2021, **405**, 126951.
14 Y. Chen, X. He, D. Guo, Y. Cai, J. Chen, Y. Zheng, B. Gao, B. Lin, *J. Energy Chem.*, 2020, **49**, 214.
15 B. Jürgens, E. Irran, J. Senker, P. Kroll, H. Müller, W. Schnick, *J. Am. Chem. Soc.*, 2003, **125**, 10288.
16 H. B. Zheng, W. Chen, H. Gao, Y. Y. Wang, H. Y. Guo, S. Q. Guo, Z. L. Tang, J. Y. Zhang, *J. Mater. Chem. C*, 2017, **5**, 10746.
17 E. Kroke, M. Schwarz, E. Horath-Bordon, P. Kroll, B. Noll, A. D. Norman, *New J. Chem.*, 2002, **26**, 508.
18 S. Chu, C. Wang, J. Feng, Y. Wang, Z. Zou, *Int. J. Hydrogen Energy*, 2014, **39**, 13519.
19 Z. Huang, F. -W. Yan, G. -q. Yuan, *ACS Sustainable Chem. Eng.*, 2018, **6**, 3187.
20 Z. Mo, H. Xu, Z. Chen, X. She, Y. Song, J. Wu, P. Yan, L. Xu, Y. Lei, S. Yuan, H. Li, *Appl. Catal. B*, 2018, **225**, 154.
21 J. Xia, N. Karjule, B. Mondal, J. Qin, M. Volokh, L. Xing, M. Shalom, *J. Mater. Chem. A*, 2021, **9**, 17855.
22 J. Xia, N. Karjule, L. Abisdris, M. Volokh, M. Shalom, *Chem. Mater.*, 2020, **32**, 5845.
23 L. Zhu, X. Xu, Y.A.N. Wang, S. Liu, J. I. E. Ling, L. Liu, S. Wei, F. Cai, Z. Wang, X. Liu, L. I. Wang, *Surf. Rev. Lett.*, 2014, **21**, 1450035.
24 J. Xu, L. Zhang, R. Shi, Y. Zhu, *J. Mater. Chem. A*, 2013, **1**, 14766.
25 X. Du, G. Zou, Z. Wang, X. Wang, *Nanoscale*, 2015, **7**, 8701.
26 F. Cheng, H. Wang, X. Dong, *Chem. Commun.*, 2015, **51**, 7176.
27 J. Wen, R. Li, R. Lu, A. Yu, *Chem. Asian J.*, 2018, **13**, 1060.
28 S. Uemura, K. Sakata, M. Aono, Y. Nakamura, M. Kunitake, *Front. Chem. Sci. Eng.*, 2016, **10**, 294.
29 A. Sattler, W. Schnick, Z. Anorg.Allg. *Chem.*, 2010, 636, 2589.
30 A. Sattler, L. Seyfarth, J. Senker, W. Schnick, *Z. Anorg. Allg. Chem.*, 2005, **631**, 2545.
31 H. Y. Yuan, J. Y. Bai, B. Xu, X. Y. Li, S. Y. Xiao, P. F. Liu, X. L. Wang, H. G. Yang, *Chem. Commun.*, 2021, **57**, 3042.
32 W. Yu, T. Zhang, Z. Zhao, *Appl. Catal. B*, 2020, **278**, 119342.
33 C. Wang, G. Liu, K. Song, X. Wang, H. Wang, N. Zhao, F. He, *ChemCatChem*, 2019, **11**, 6364.
34 Z. Pan, P. Niu, M. Liu, G. Zhang, Z. Zhu, X. Wang, *ChemSusChem*, 2020, **13**, 888.
35 Y. Li, S. Wang, W. Chang, L. Zhang, Z. Wu, S. Song, Y. Xing, *J. Mater. Chem. A*, 2019, **7**, 20640.
36 P. Luan, Q. Meng, J. Wu, Q. Li, X. Zhang, Y. Zhang, L. A. O'Dell, S. R. Raga, J. Pringle, J. C. Griffith, C. Sun, U. Bach, J. Zhang, *ChemSusChem*, 2020, **13**, 328.
37 Q. Liu, C. Chen, K. Yuan, C.D. Sewell, Z. Zhang, X. Fang, Z. Lin, *Nano Energy*, 2020, **77**, 105104.
38 C. Cheng, L. Mao, Z. Huang, J. Shi, B. Zheng, Y. Zhang, L. Guo, *J. Colloid Interface Sci.*, 2021, **601**, 220.
39 Q. Liu, J. Shen, X. Yu, X. Yang, W. Liu, J. Yang, H. Tang, H. Xu, H. Li, Y. Li, J. Xu, *Appl. Catal. B*, 2019, **248**, 84.
40 J. Huang, H. Wang, H. Yu, Q. Zhang, Y. Cao, F. Peng, *ChemSusChem*, 2020, **13**, 5041.
41 H. Miao, J. Yang, Y. Sheng, W. Li, Y. Zhu, *Sol. RRL*, 2020, 2000453.
42 S. Liu, Z. Wang, Y. Lu, H. Li, X. Chen, G. Wei, T. Wu, D. -J. Maguire, G. Ye, J. Chen, *Appl. Catal. B*, 2021, **282**, 119523.

43 J. Ran, H. Zhang, J. Qu, J. Shan, S. Chen, F. Yang, R. Zheng, J. Cairney, L. Song, L. Jing, S.-Z. Qiao, *ACS Materials Lett.*, 2020, **2**, 1484.
44 Y. Zhang, D. Yao, B. Xia, H. Xu, Y. Tang, K. Davey, J. Ran, S.-Z. Qiao, *Small Sci.*, 2021, **1**, 2000052.
45 Y. Zhang, B. Xia, J. Ran, K. Davey, S.Z. Qiao, *Adv. Energy Mater.*, 2020, **10**, 1903879.
46 J. Sun, F. Yao, L. Dai, J. Deng, H. Zhao, L. Zhang, Y. Huang, Z. Zou, Y. Fu, J. Zhu, *ACS Appl. Mater. Interfaces*, 2020, **12**, 40433.
47 . Yang, G. Zeng, D. Huang, C. Zhang, D. He, C. Zhou, W. Wang, W. Xiong, X. Li, B. Li, W. Dong, Y. Zhou, *Appl. Catal. B*, 2020, **272**, 118970.

Electronic Supplementary Information

Supramolecular organization of melem for the synthesis of photoactive porous carbon nitride rods

Jiawei Xia,[a,b] Gabriel Mark,[b] Michael Volokh,[b] Yuanxing Fang,[c] Haiqun Chen,[a] Xinchen Wang[c] and Menny Shalom[b]*

[a]Key Laboratory of Advanced Catalytic Materials and Technology, Advanced Catalysis and Green Manufacturing Collaborative Innovation Center, Changzhou University, Changzhou, Jiangsu Province 213164, China.

[b]Department of Chemistry and Ilse Katz Institute for Nanoscale Science and Technology, Ben-Gurion University of the Negev, Beer-Sheva 8410501, Israel.
E-mail: mennysh@bgu.ac.il

[c]State Key Laboratory of Photocatalysis on Energy and Environment College of Chemistry, Fuzhou University, Fuzhou 350116, China

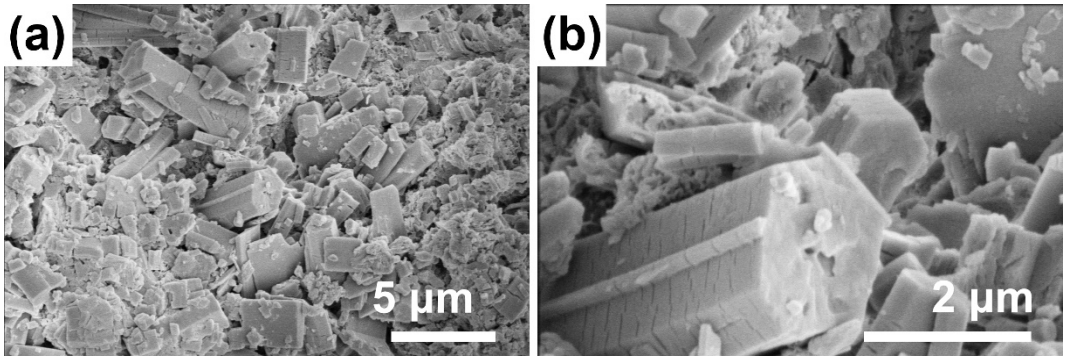

Fig. S1 SEM images of Me at different magnifications.

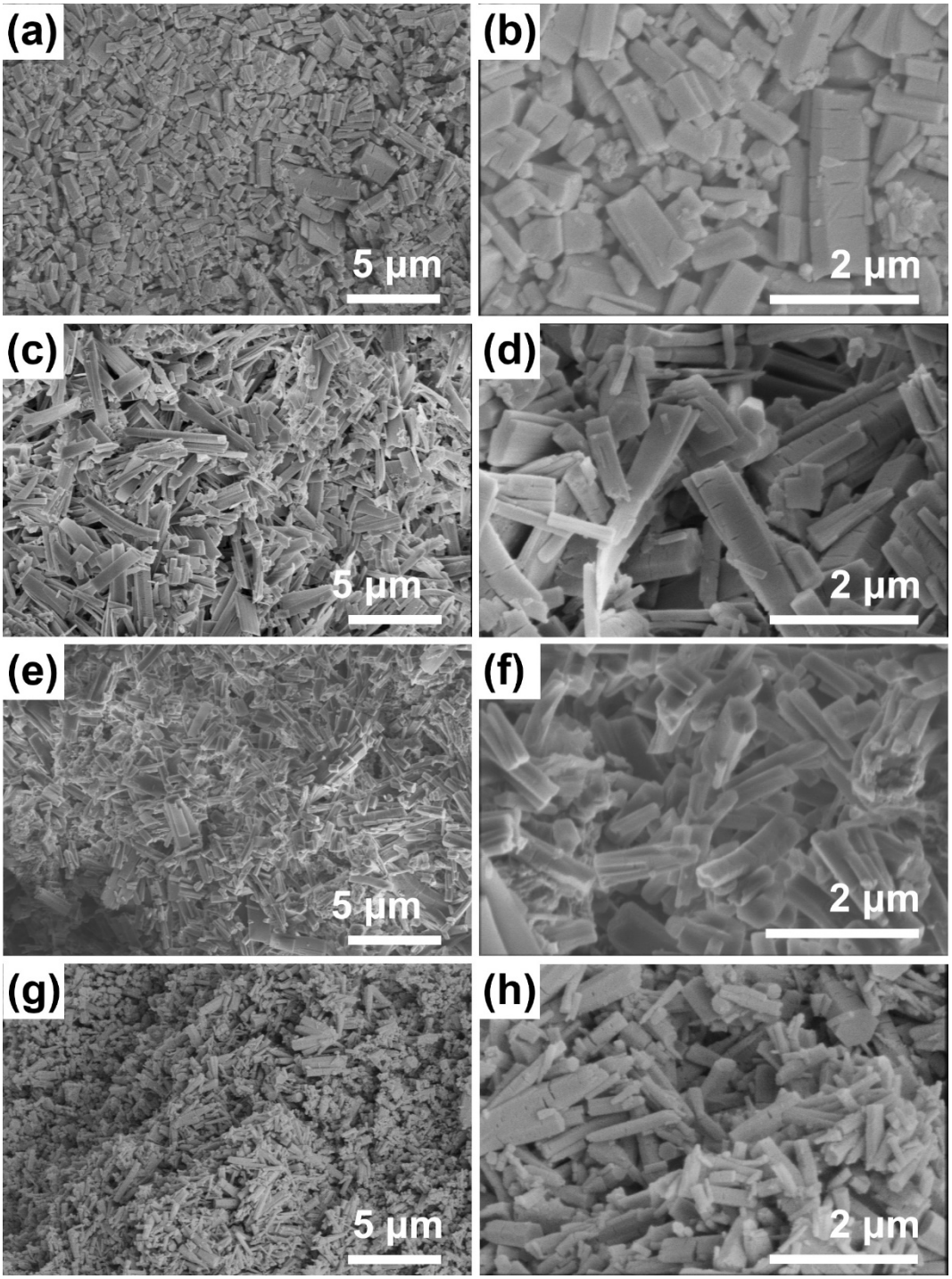

Fig. S2 SEM images of (a, b) $MeCl_{0.2}$, (c, d) $MeCl_{0.4}$, (e, f) $MeCl_{0.6}$, and (g, h) $MeCl_{0.8}$ at different magnifications.

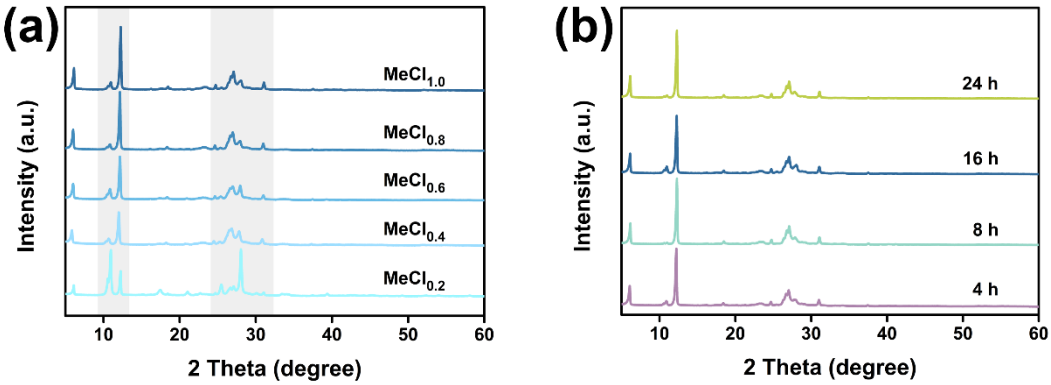

Fig. S3 (a) XRD patterns of $MeCl_x$ synthesized in aqueous solutions of different HCl concentrations; (b) XRD patterns of $MeCl_{1.0}$ synthesized with different shaking times.

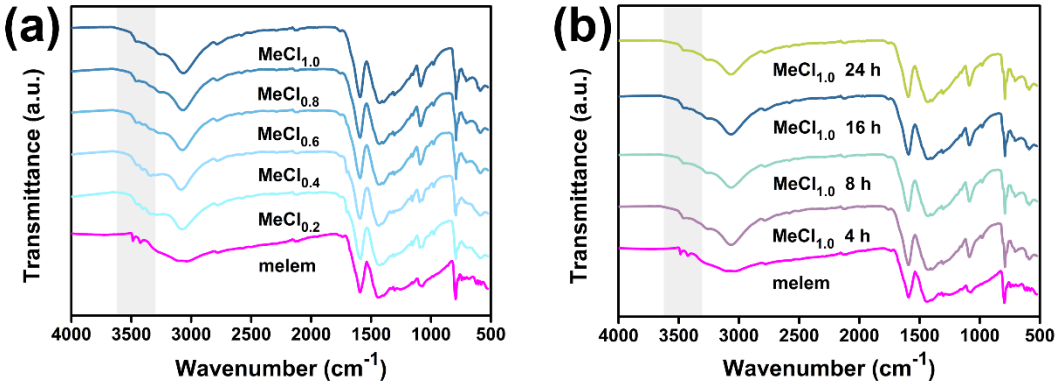

Fig. S4 (a) FTIR spectra of $MeCl_x$ synthesized in aqueous solutions of different HCl concentrations; (b) FTIR spectra of $MeCl_{1.0}$ synthesized with different shaking times. Untreated bulk melem for comparison (bottom, magenta spectra)

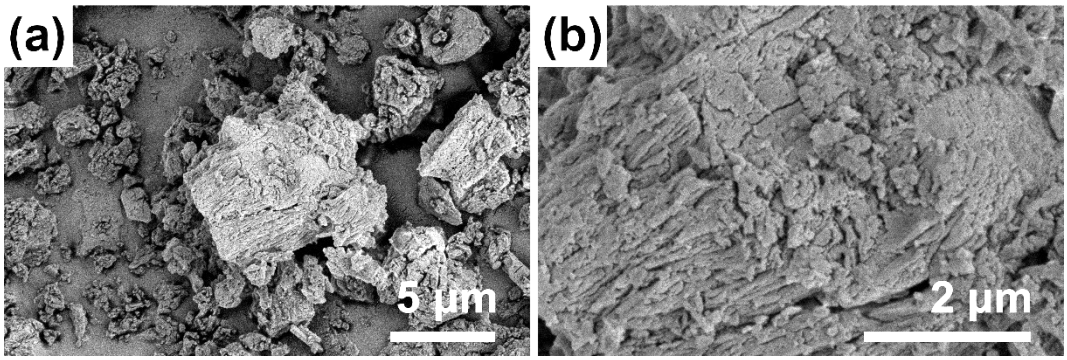

Fig. S5 SEM images of unwashed HCl-treated melem (melem+HCl) at different magnifications.

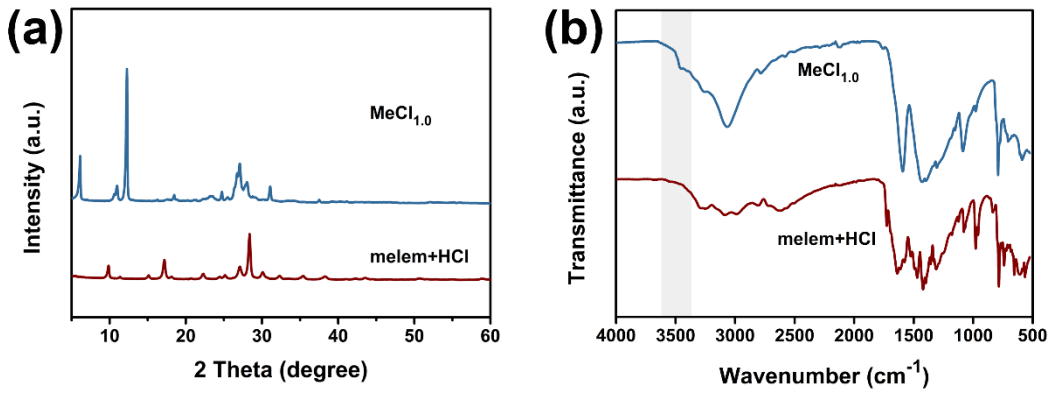

Fig. S6 (a) XRD patterns and (b) FTIR spectra of $MeCl_{1.0}$ and unwashed HCl-treated melem (melem+HCl).

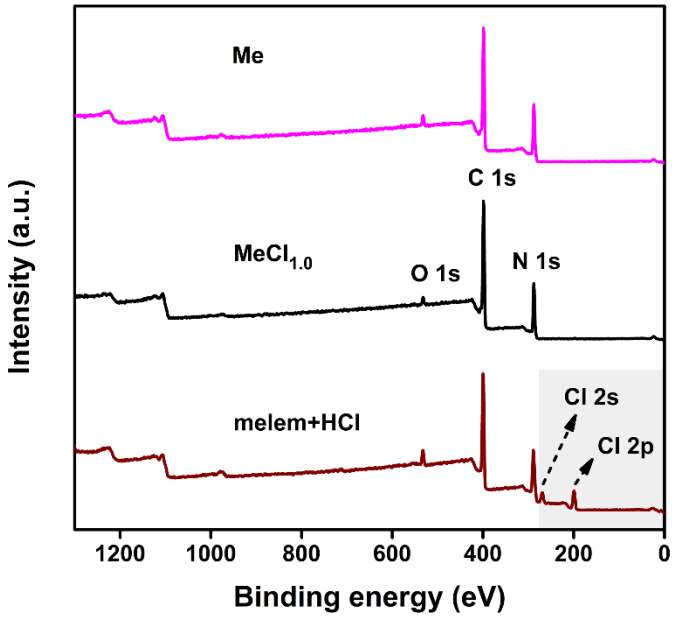

Fig. S7 Global XPS spectra of Me, $MeCl_{1.0}$, and melem+HCl.

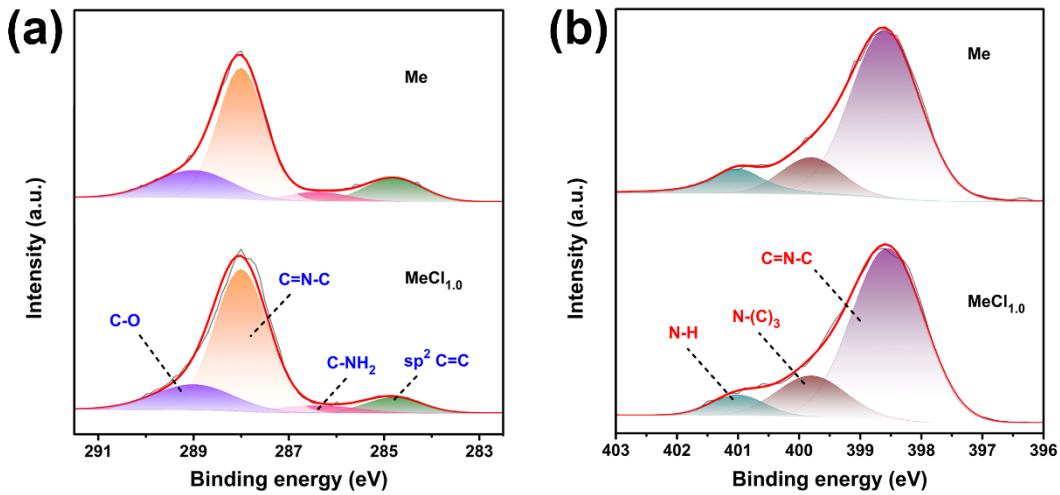

Fig. S8 (a) C 1s and (b) N 1s high-resolution XPS spectra of Me and $MeCl_{1.0}$.

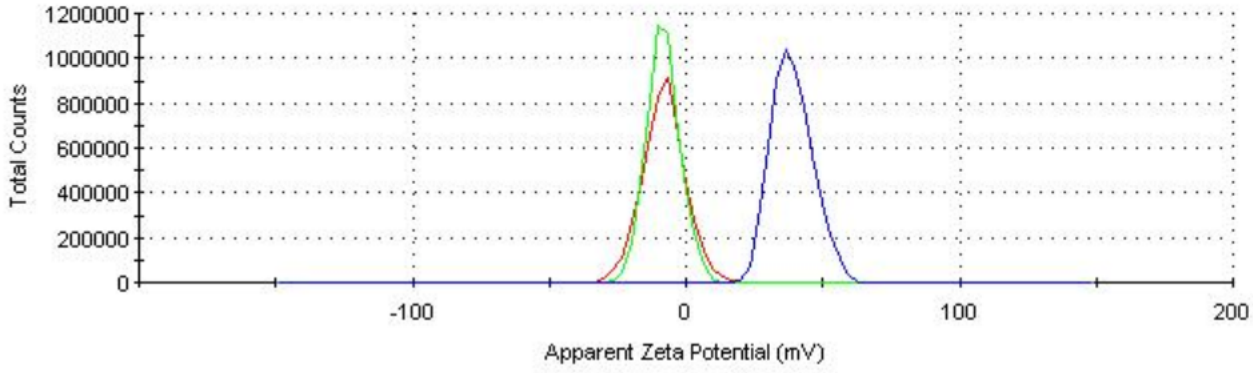

Fig. S9 Zeta-potential measurements of Me (green), $MeCl_{1.0}$ (red), and melem+HCl (blue) aqueous suspensions.

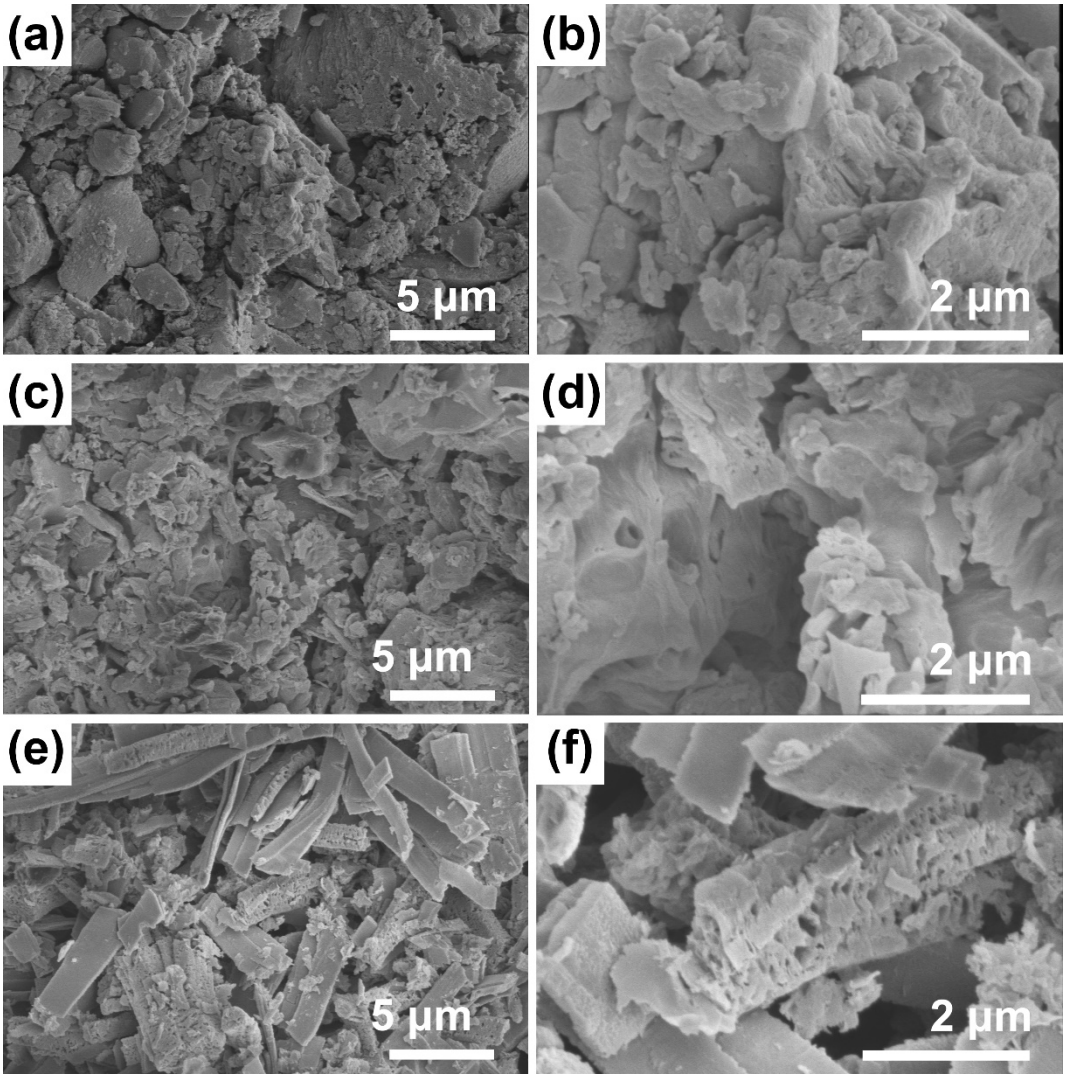

Fig. S10 SEM images of (a, b) CN-M, (c, d) CN-melem, and (e, f) CN-Me at different magnifications.

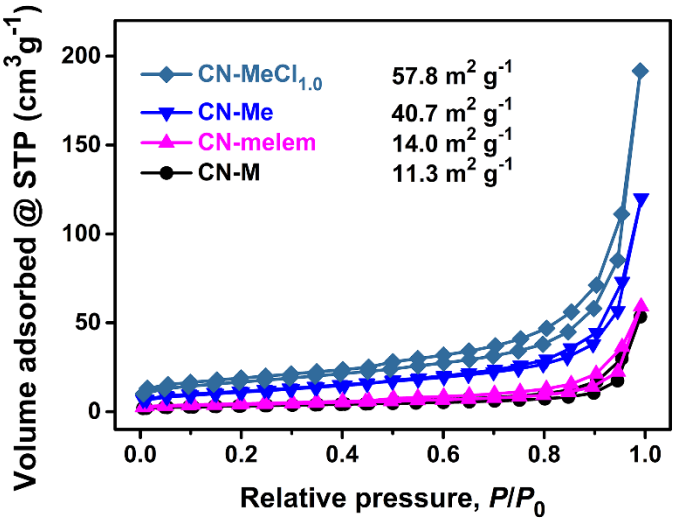

Fig. S11 Nitrogen adsorption-desorption isotherms (77 K) and specific surface area analysis according to the Brunauer-Emmett-Teller (BET) model.

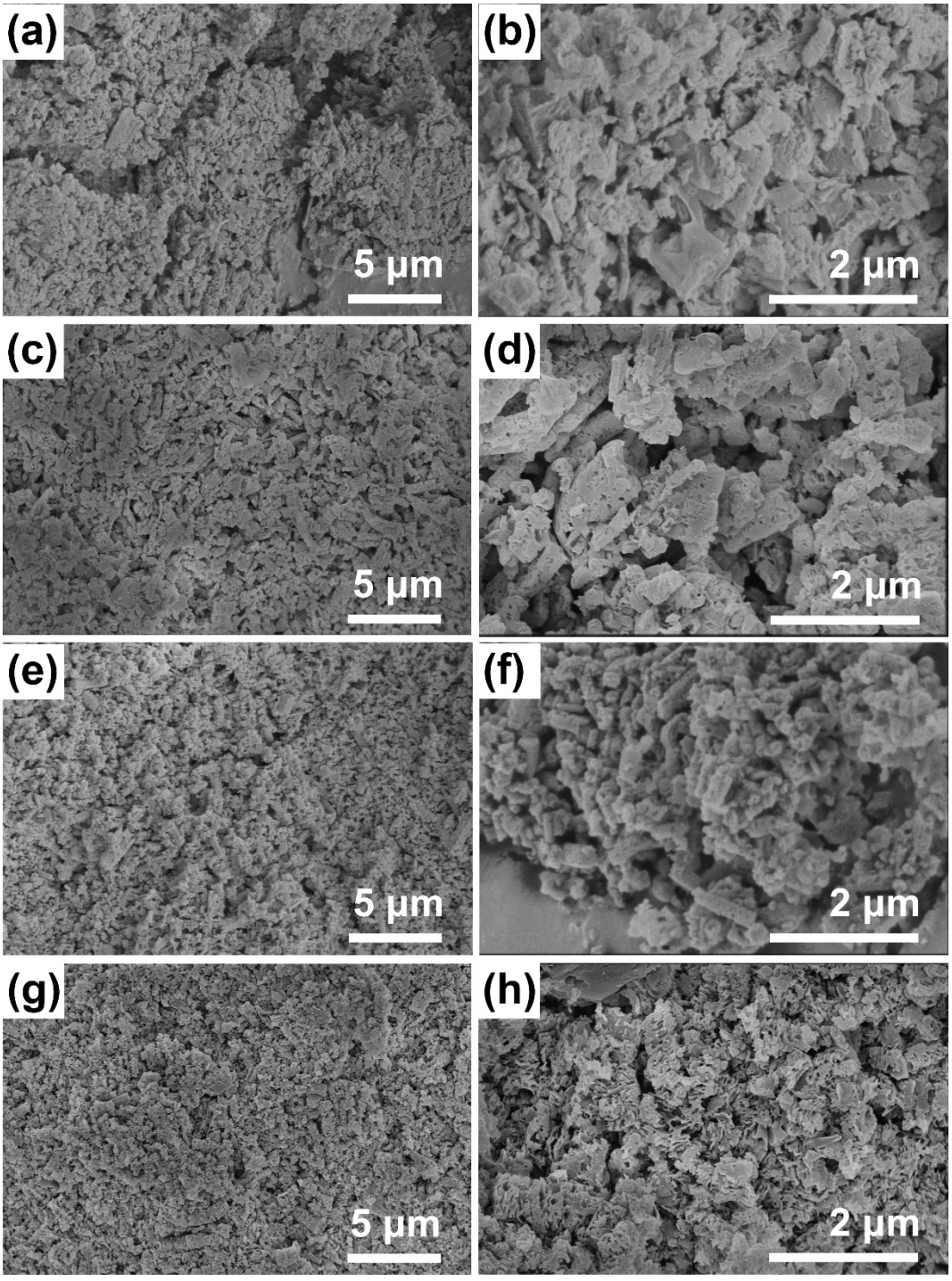

Fig. S12 SEM images of (a, b) CN-$MeCl_{0.2}$, (c, d) CN-$MeCl_{0.4}$, (e, f) CN-$MeCl_{0.6}$, and (g, h) CN-$MeCl_{0.8}$ at different magnifications.

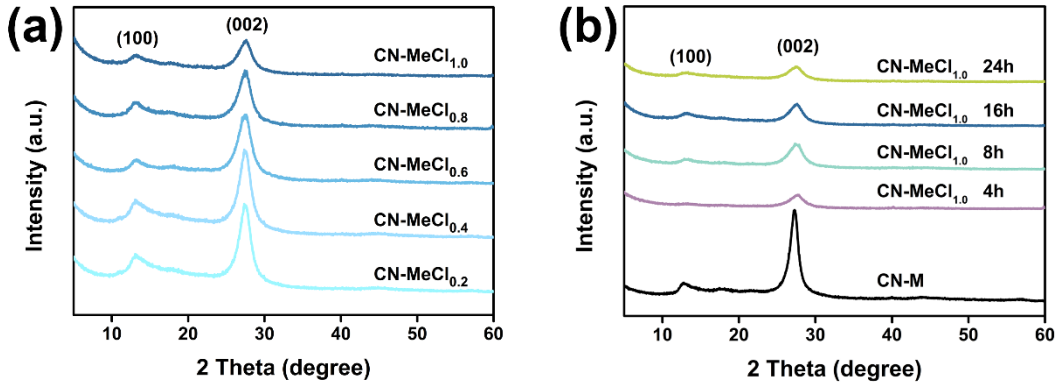

Fig. S13 (a) XRD patterns of CN materials from $MeCl_x$, synthesized in aqueous solutions of different HCl concentrations; (b) XRD patterns of CN-M compared with CN materials from $MeCl_{1.0}$ synthesized with different shaking times.

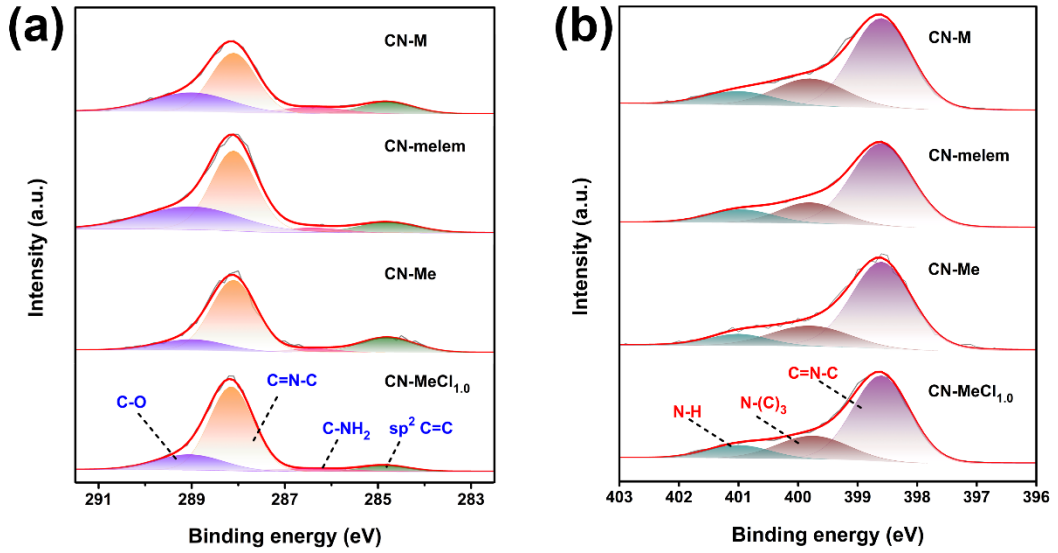

Fig. S14 (a) C 1s and (b) N 1s high-resolution XPS spectra of CN-M, CN-melem, CN-Me, and CN-$MeCl_{1.0}$.

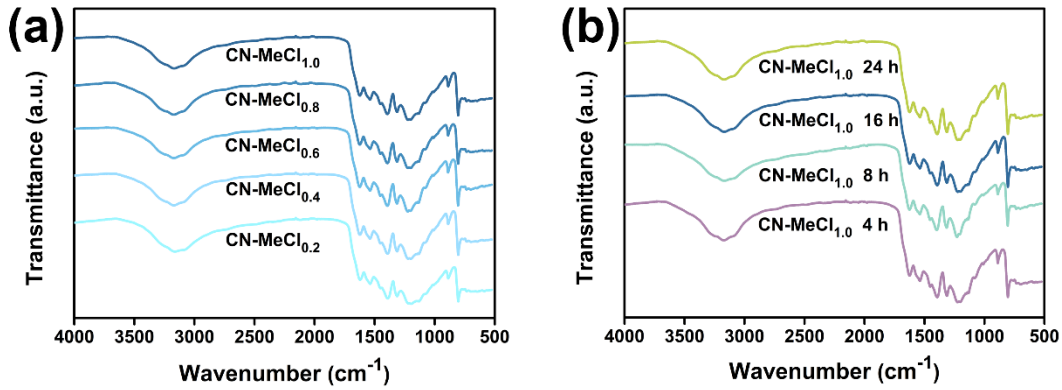

Fig. S15 (a) FTIR spectra of CN materials from $MeCl_x$, synthesized in aqueous solutions of different HCl concentrations; (b) FTIR spectra of CN materials from $MeCl_{1.0}$ synthesized with different shaking times.

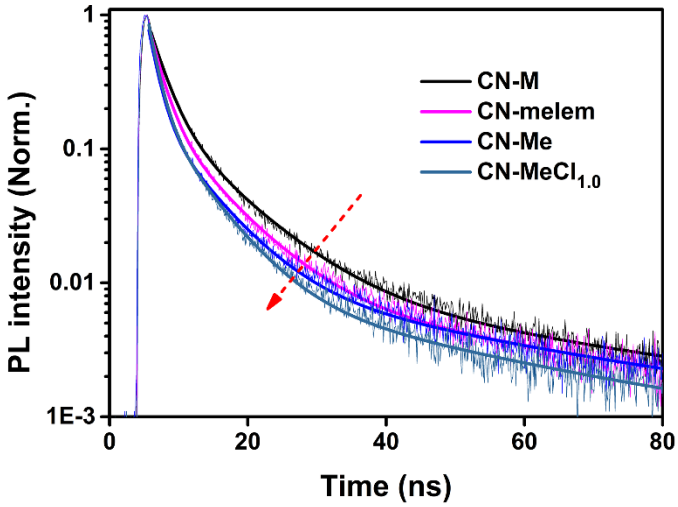

Fig. S16 Normalized time-resolved PL decay spectra of different CN materials (all samples were excited at λ_{ex} = 370 nm).

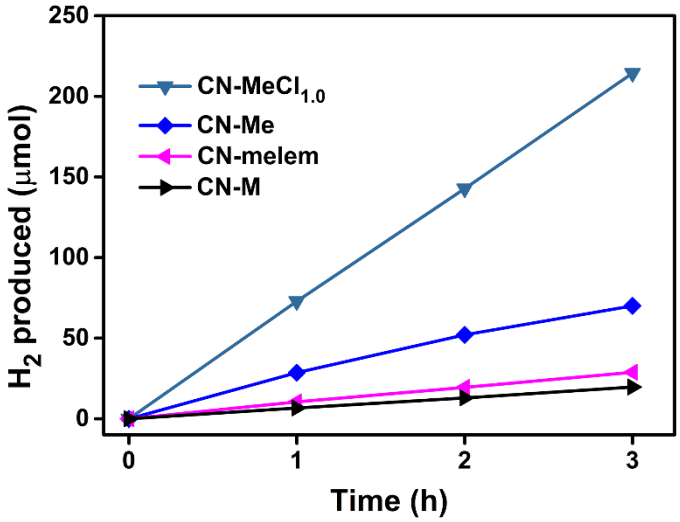

Fig. S17 Time course of H_2 evolution under white LED irradiation, catalyzed by different CN materials.

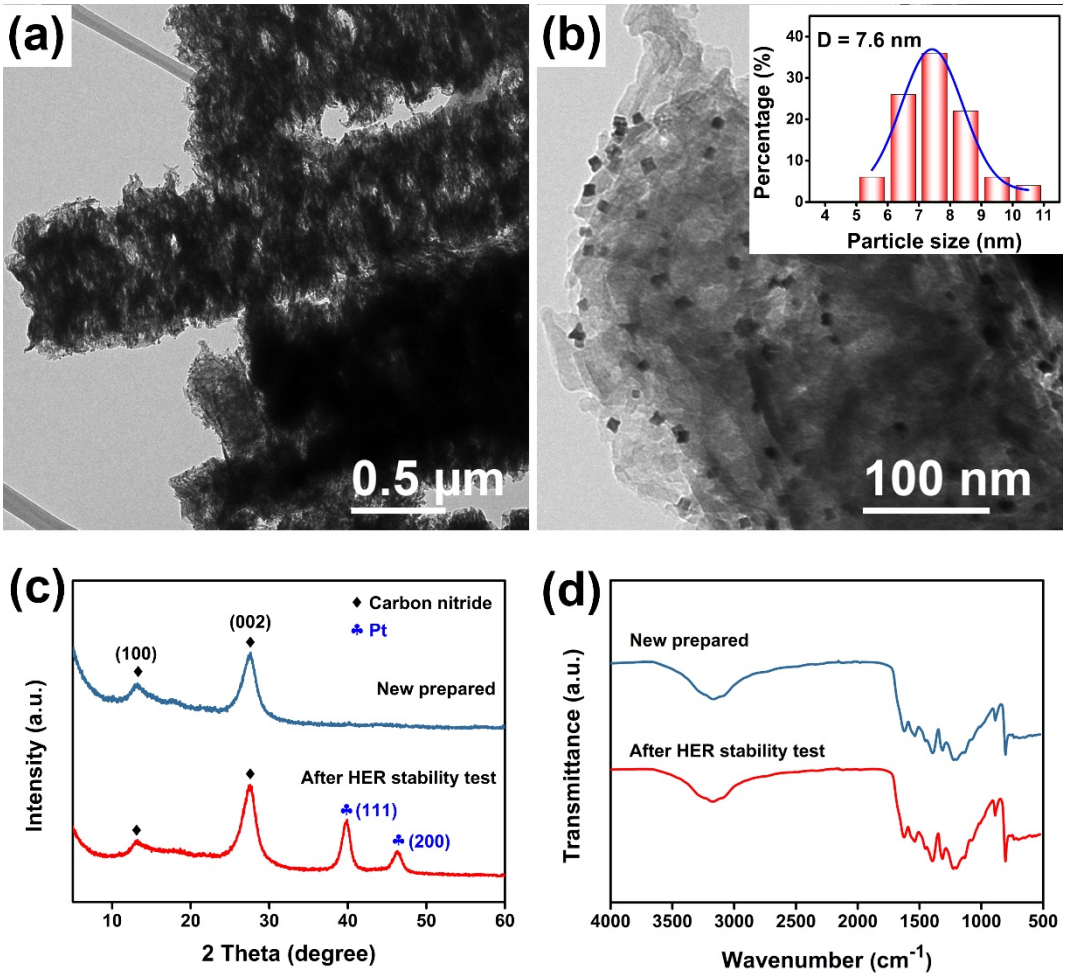

Fig. S18 (a,b) TEM images of CN-$MeCl_{1.0}$ at two different magnifications after an HER stability test. The inset in (b) presents a size distribution historgram of Pt nanoparticles; (c) XRD patterns and (d) FTIR spectra of CN-$MeCl_{1.0}$ before and after HER stability test.

The two diffraction peaks located at 2θ = 39.8° and 2θ = 46.2° are assigned to the (111) and (200) planes of face center cubic (fcc) Pt nanoparticles, which are photodeposited onto the surface of CN material. The XRD patterns and FTIR spectra of CN-$MeCl_{1.0}$ do not reveal noticeable change before and after HER stability test, indicating a good structural stability.

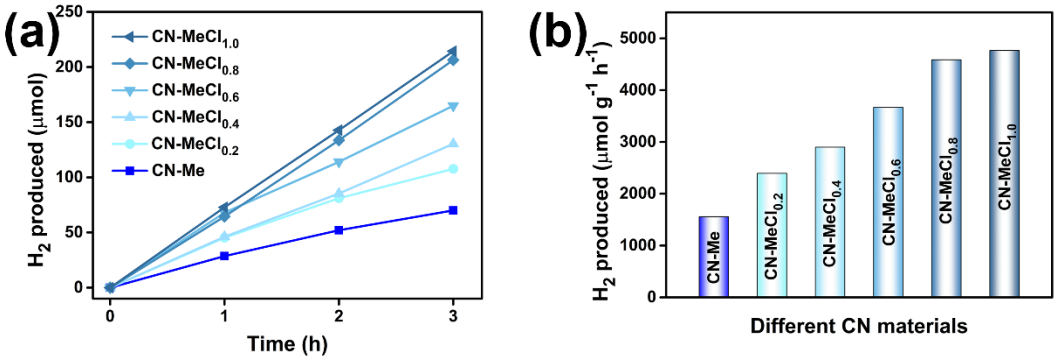

Fig. S19 (a) Time course of H_2 evolution under white LED irradiation, catalyzed by CN materials synthesized in aqueous solutions of different HCl concentrations; (b) The corresponding HER rate at the 3rd hour.

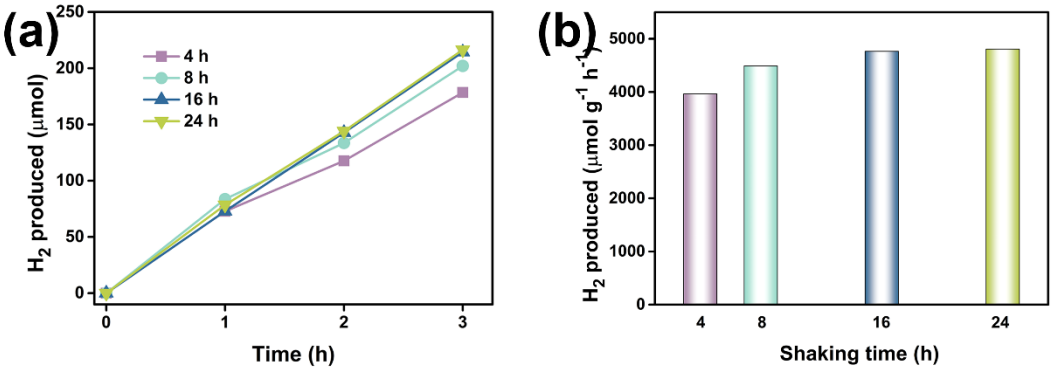

Fig. S20 (a) Time course of H_2 evolution under white LED irradiation, catalyzed by CN materials synthesized from $MeCl_{1.0}$ with different shaking times; (b) Corresponding HER rate at the 3rd hour.

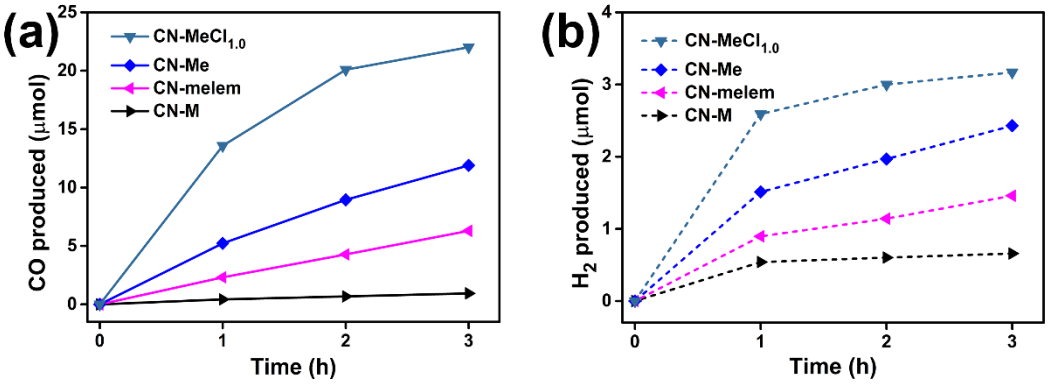

Fig. S21 Time course of generated (a) CO and (b) H_2 under white LED irradiation, catalyzed by different CN materials.

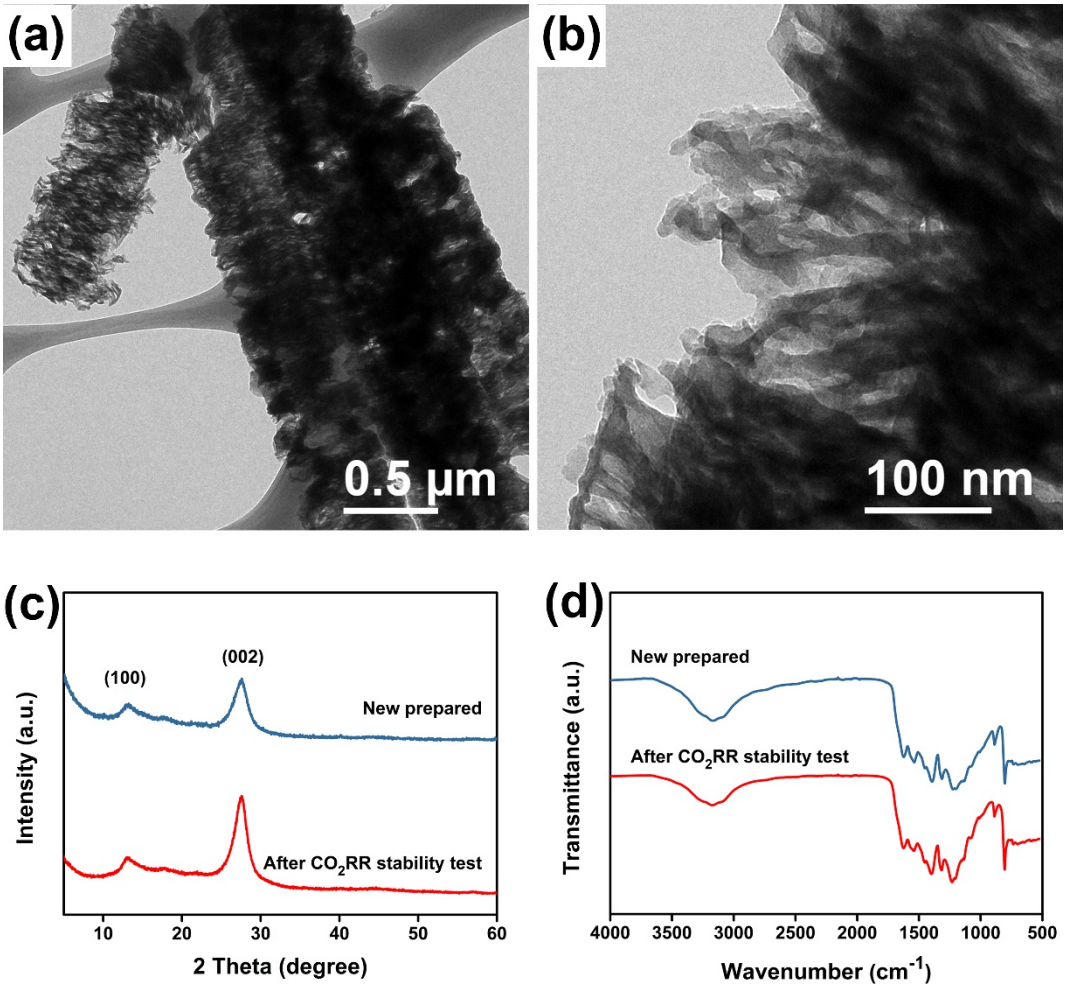

Fig. S22 (a, b) TEM images of CN-$MeCl_{1.0}$ after CO_2RR stability test at two different magnifications; (c) XRD patterns and (d) FTIR spectra of CN-$MeCl_{1.0}$ before and after CO_2RR stability test.

The XRD patterns and FTIR spectra of CN-$MeCl_{1.0}$ do not reveal a noticeable change before and after a HER stability test, indicating a good structural stability.

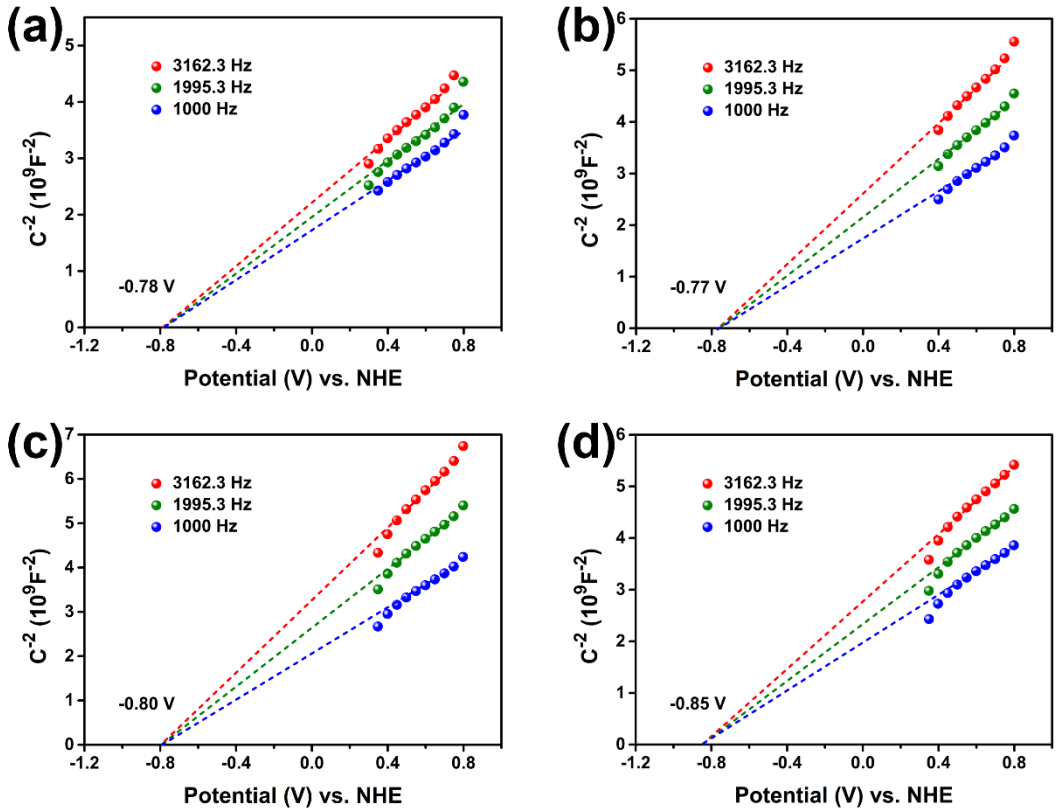

Fig. S23 Mott-Schottky plots of (a) CN-M, (b) CN-melem, (c) CN-Me, and (d) CN-$MeCl_{1.0}$, measured in 1.0 M Na_2SO_4 aqueous solution as the electrolyte.

Table S1. PL lifetimes estimated from time-resolved PL spectra decay curves according to a triple-exponential function fitting.

Catalyst	τ_1 (ns)	A_1 (%)	τ_2 (ns)	A_2 (%)	τ_3 (ns)	A_3 (%)	$\tau_{av.}$ (ns)
CN-M	8.24	45.91	49.53	16.33	2.16	37.76	34.17
CN-melem	1.75	35.87	7.11	47.19	45.64	16.95	32.26
CN-Me	1.32	24.24	6.17	46.86	39.03	18.91	28.58
CN-$MeCl_{1.0}$	5.68	47.33	34.98	14.91	1.32	37.76	23.61

The PL lifetimes ($\tau_{av.}$) were estimated from time-resolved PL spectra decay curves fitted to a triple-exponential function: $\tau = \sum_{i=1}^{i=n} A_i \tau_i^2 / \sum_{i=1}^{i=n} A_i \tau_i$, where τ_i is the lifetime and A_i is the amplitude of the i^{th} component.

Table S2. Comparison of the properties of CN materials used as HER photocatalysts

Catalyst	Method	Light source	Catalyst mass	Experimental conditions	Hydrogen evolution rate (μmol g^{-1} h^{-1})	AQE (%)	Ref.
CN from melem-based supramolecular hexagonal rods	Supramolecular assembly of melem exfoliated by HCl, followed by thermal condensation	100 W white LED (λ > 410 nm), water bath	15 mg	3 wt.% Pt, 10 vol.% TEOA	4764	6.8 (λ = 405 nm)	This work
Porous CN	Thermal condensation of melamine-halogen complex	50 W white LED (λ > 410 nm)	15 mg	3 wt.% Pt, 10% vol.% TEOA	1815	3.2 (λ = 405 nm)	[1]
Hierarchical rod-like graphitic CN	Ultrasound-assisted supramolecular assembly of melem, followed by thermal condensation	300 W Xe lamp (λ > 420 nm)	100 mg	3 wt.% Pt, 10% vol.% TEOA	2460	—	[2]
Graphene-like CN rich in N vacancies	Thermal polymerization of melamine using graphene oxide as a sacrificial template	300 W Xe lamp (λ > 420 nm)	100 mg	3 wt.% Pt, 25% vol.% methanol	3171	~6 (λ = 421 nm)	[3]
High crystalline CN	Rapid polymerization of melamine powder	300 W Xe lamp (λ > 420 nm)	50 mg	3 wt.% Pt, 10 vol.% TEOA	339.4	3.8 (λ = 420 nm)	[4]
Macroscopic foam-like holey ultrathin CN nanosheets	Self-modification of polymeric melon units through long-time thermally treating bulk g-C_3N_4 under an air atmosphere	300 W Xe lamp (λ > 400 nm)	20 mg	3 wt.% Pt, 10 vol.% TEOA	1144	4.03 (λ = 420±15 nm)	[5]
Crystalline CN	Condensation of melamine powder, followed by a sequential heating in KCl-LiCl mixed sault	300 W Xe lamp	50 mg	3 wt.% Pt, 10 vol.% TEOA	1280	~6.0 (λ = 405 nm)	[6]
Holey CN nanosheets	Condensation of melamine powder in a big crucible with empty space covered with two Z204 catalysts	300 W Xe lamp (λ > 400 nm)	50 mg	3 wt.% Pt, 10 vol.% TEOA	2320	—	[7]
Defect engineering-modified atomic layered CN	High-temperature treatment and the two-step thermal exfoliation process	Xe lamp (λ > 420 nm)	50 mg	3 wt.% Pt, 10 vol.% TEOA	3700	14.98 (λ > 420 nm)	[8]
Polymeric CN nanotubbes	Condensation of trithiocyanuric acid-melamine supramolecular assembly, followed by further heating treatment in NaCl salt	300 W Xe lamp (λ > 420 nm)	50 mg	1 wt.% Pt, 10 vol.% TEOA	4350	3.34 (λ = 420 nm)	[9]
Phenyl-bridged porous and hollow CN sphere	Condensation of trimesic acid-doped cyanuric acid-melamine supramolecular assembly	300 W Xe lamp (λ > 400 nm)	20 mg	3 wt.% Pt, 10 vol.% TEOA	4455	—	[10]

Electronic Supplementary Information References

[1] J. Barrio, A. Grafmüller, J. Tzadikov, M. Shalom, *Appl. Catal. B*, 2018, **237**, 681.

[2] Z. Huang, F. -W. Yan, G. -q. Yuan, *ACS Sustainable Chem. Eng.*, 2018, **6**, 3187.

[3] R. Wang, X. Wang, X. Li, L. Pei, X. Gu, Z. Zheng, *Int. J. Hydrogen Energy*, 2021, **46**, 197.

[4] L. Wang, Y. Hong, E. Liu, Z. Wang, J. Chen, S. Yang, J. Wang, X. Lin, J. Shi, *Int. J. Hydrogen Energy*, 2020, **45**, 6425.

[5] Y. Li, R. Jin, Y. Xing, J. Li, S. Song, X. Liu, M. Li, R. Jin, *Adv. Energy Mater.*, 2016, **6**, 1601273.

[6] W. Ren, J. Cheng, H. Ou, C. Huang, M.M. Titirici, X. Wang, *ChemSusChem*, 2019, **12**, 3257.

[7] G. Li, Z. Xie, S. Chai, X. Chen, X. Wang, *Appl. Catal. B*, 2021, **283**, 119637.

[8] J. Zhang, J. Chen, Y. Wan, H. Liu, W. Chen, G. Wang, R. Wang, *ACS Appl. Mater. Interfaces*, 2020, **12**, 13805.

[9] Y. Wan, J. Zhang, J. Chen, Z. Liu, J. Fan, J. Zhang, G. Wang, R. Wang, *Chem. Eng. J.*, 2021, **417**, 127956.

[10] Y. Chen, Y. Qu, X. Zhou, D. Li, P. Xu, J. Sun, *ACS Appl. Mater. Interfaces*, 2020, **12**, 41527.